The International Journal of Advanced Manufacturing Technology (2023) 125:1511–1529
https://doi.org/10.1007/s00170-022-10658-6

ORIGINAL ARTICLE

Developing the optimized control scheme for continuous and layer-wise DLP 3D printing by CFD simulation

Lidong Zhao[1] · Yan Zhang[2] · Lifang Wu[1] · Zhi Zhao[3] · Zening Men[1] · Feng Yang[1]

Received: 15 July 2022 / Accepted: 4 December 2022 / Published online: 9 January 2023

Abstract

In recent years, a series of continuous fabrication technologies based on digital light processing (DLP) 3D printing have emerged, which have significantly improved the speed of 3D printing. However, limited by the resin filling speed, those technologies are only suitable to print hollow structures. In this paper, an optimized protocol for developing continuous and layer-wise hybrid DLP 3D printing mode is proposed based on computational fluid dynamics (CFD). Volume of the fluid method is used to simulate the behavior of resin flow while Poiseuille flow, Jacobs working curve, and Beer-Lambert law are used to optimize the key control parameters for continuous and layer-wise printing. This strategy provides a novel simulation-based method development scenario to establish printing control parameters that are applicable to arbitrary structures. Experiments verified that the printing control parameters obtained by simulations can effectively improve the printing efficiency and the applicability of DLP 3D printing.

Keywords DLP 3D printing · Computational fluid dynamics · Layer-wise printing · Continuous printing · Control parameters · Resin filling

✉ Lifang Wu
lfwu@bjut.edu.cn

Lidong Zhao
ldzhao817@126.com

Yan Zhang
zhangyan162@imech.ac.cn

Zhi Zhao
zhaozhi@bjut.edu.cn

Zening Men
menzening@163.com

Feng Yang
yangf_186389@163.com

[1] Faculty of Information Technology, Beijing University of Technology, 100 Pingleyuan, Chaoyang District, Beijing, 100124, China

[2] Institute of Mechanics, Chinese Academy of Sciences, No.15 Beisihuanxi Road, Beijing, 100190, China

[3] Faculty of Materials and Manufacturing, Beijing University of Technology, 100 Pingleyuan, Chaoyang District, Beijing, 100124, China

1 Introduction

Additive manufacturing (AM), also known as 3D printing, is a novel technology that is much different from traditional manufacturing technologies. AM is usually used to manufacture products with complex structures [1–3], which shows wide applications in manufacturing, medicine, education, aerospace, and other fields [4]. However, the production speed of AM is much lower than that of traditional manufacturing technology. Therefore, it is impractical to manufacture a large number of products by 3D printing [5].

In recent years, digital light processing (DLP)-based continuous 3D printing has been proposed, which shows significant improvement in printing speed. The key to continuous printing is to a spontaneous detachment of cured parts from the resin vat [6]. According to the working principle, DLP-based continuous 3D printing techniques could be briefly classified into two categories, namely those based on selective inhibition of polymerization and the ones relying on low adhesive interfaces [7]. The former methods utilized wavelength-selective inhibitors or initiators to chemically separate cured resins from the optical window

[8, 9]. Alternatively, the latter approaches introduced a low adhesion interface to physically prevent cured parts from sticking to the resin vat, which typically included oxygen-permeable windows [10], fluorinated oil beds [11], and biomimetic ultra-low adhesive interfaces [12]. Among them, the method based on fluorinated oil bed could effectively dissipate accumulated heat during continuous printing, enabling large-scale product production. However, Li et al. [13] found that most continuous printing methods could only guarantee a complete resin filling for microscopically sized features due to the limited fluidity of resins. Consequently, continuous printing methods were majorly used to print hollow structures [13–15], as shown in Fig. 1a. On the other hand, most practical applications demand structures with alternative hollow and solid moieties (as shown in Fig. 1b and c) or pure solid structures (as shown in Fig. 1d and e). Obviously, it is impossible to print such models directly using continuous printing technologies.

To address the above issues, Liu et al. [16] and Li et al. [17] proposed the idea of combining continuous and layer-wise printing. They obtained the resin materials' maximum filled distance (MFD) by experiments. Based on that, features to be printed in continuous mode and layer-wise mode in a given model can be determined. Despite their success, obtaining a control scheme from experiments is very time consuming. Considering the experimental accuracy, the as-obtained control parameters may not be optimal, either.

In recent years, some effective schemes have been proposed to improve the applicability of continuous optical printing by theoretical analysis based on material science and physical field model. Wang et al. [18] simulated the behavior of resin flow in the micro-gap between the newly cured layer and the oxygen permeable window in CLIP by using computational fluid dynamics (CFD) analysis. Based on the simulation results, they proposed some suggestions for optimizing operational conditions. Lee et al. [19] studied common problems in the layer-wise DLP 3D printing process based on a finite element mesh generator and optimized printing control parameters. Li et al. [20] proposed a differential analysis model for DLP 3D printing based on the Jacobs working curve, which was used to obtain the relationship between the UV light irradiation time and the curing thickness of a single layer. The model could optimize the printing control parameters and achieve high-precision printing. Brighenti et al. [21] proposed a multi-physics simulation method for DLP 3D printing to predict the mechanical features of additively manufactured parts and accurately control the polymerization. To optimize the printing process, Wang et al. [22] established a dynamic model of the oxygen inhibition zone in CLIP to study how the thickness of the oxygen-inhibited zone varied with regard to the printing control parameters and the microstructure. These studies demonstrated that the setting and optimization of DLP 3D printing parameters based on physics simulation could improve the optimization efficiency of printing control parameters. Furthermore, when the simulation conditions were close to the actual situations, the control parameters obtained based on the simulation were meaningful and practical for actual printing process [23].

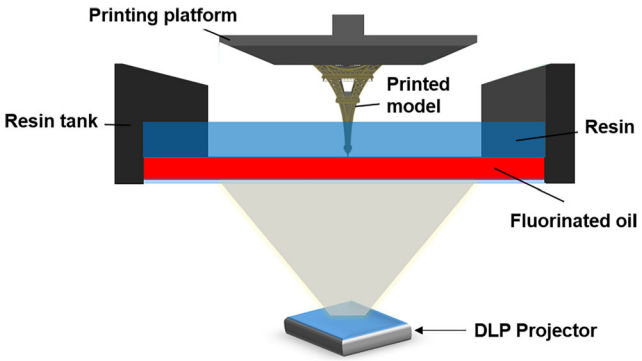

Fig. 2 Schematic diagram of printing scene based on the non-adhesive fluorinated oil bed

Fig. 1 Examples of different types of models. **a** The hollow structure model. **b** The model of the Eiffel Tower is a mainly hollow structure. **c** The model of a communication tower is the combination of hollow and solid structure. **d** The dental model is a mainly solid structure. **e** The femur model is a mainly solid structure

Inspired by the above work, we propose a scheme based on fluid dynamics simulation to design the control parameters of DLP printing to enable the fabrication of arbitrary structures by hybrid continuous and layer-wise printing. Through CFD and material property analysis, a numerical model is established by using the volume of the fluid (VOF) method, which can capture the motion characteristics of the fluid interface. With the help of Poiseuille flow, Jacobs working curve, and Beer-Lambert law, key parameters including resin curing time, maximum filled distance (MFD) for continuous printing, optimal lifting height (OLH) for layer-wise printing, and the optimal lifting speed (OLS) of the printing platform corresponding to the two modes (continuous or layer-wise) could be estimated. Based on these parameters, the printing process could be optimized and the printing efficiency could be improved.

The contributions of this paper are as follows:

1. A CFD simulation model for DLP 3D printing is proposed. It can simulate the moving behavior of resins, fluorinated oils, the free-surface between these two-phase flows, and the interface between the cured part and the fluorinated oils. Furthermore, the phenomena such as resin material filling and liquid interface fluctuation in the printing process could be simulated, which could provide theoretical support for obtaining the optimal printing control scheme.
2. By introducing a visual monitoring module to the DLP 3D printing system, the fluctuation of the free-surface between resin and fluorinated oil can be observed, which can be used to validate the proposed model.
3. Based on the proposed model, the optimal printing control schemes for the continuous-layer-wise hybrid printing mode can be quickly generated. Printing tests revealed that the as-obtained protocol was literally applicable to any structure.

2 Materials and printing setup

2.1 Materials

1,6-Hexanediol diacrylate (HDDA, 98%), trimethylolpropane triacrylate (TMPTA, 95%), bisphenol A acrylate (99%), and aliphatic urethane acrylate (98%), were purchased from Beijing HWRK Chemical Co., Ltd. Omnirad 784 (99%) was purchased from IGM. Perfluorodecyl triethoxysilane (97%), a.k.a. the fluorinated oil, was purchased from Quzhou Dongye Chemical Technology Co., Ltd.

2.2 Numerical methods

DLP 3D printing setup based on the non-adhesive fluorinated oil bed is utilized in our work. The oil bed features adhesion to the cured part and facilitates heat dissipation, which is desirable for large-scale printing [24]. Figure 2 shows the schematic diagram of the proposed method. The DLP light source projects two-dimensional images from sliced models onto the interface between the resin and the fluorinated oil, which solidifies the liquid resin. For continuous printing, DLP keeps lighting up, and the projected images are switched at a specific rate. For layer-wise printing, DLP switches between the on (for printing) and off (for platform moving and resin filling) modes.

As mentioned earlier, the resin needed to completely refill the void space left by the rising printing platform so that the next layer could be successfully cured. If the printing platform rose slowly or in a stepwise manner, the resin could refill properly. But undoubtedly, this would increase the printing time. It would be more desirable to find the optimal printing speed for given models to improve the printing efficiency. This paper proposes a scheme to optimize the DLP 3D printing control parameters for hybrid layer-wise and continuous printing, as shown in Fig. 3. Each slice's printing mode (continuous or layer-wise) is

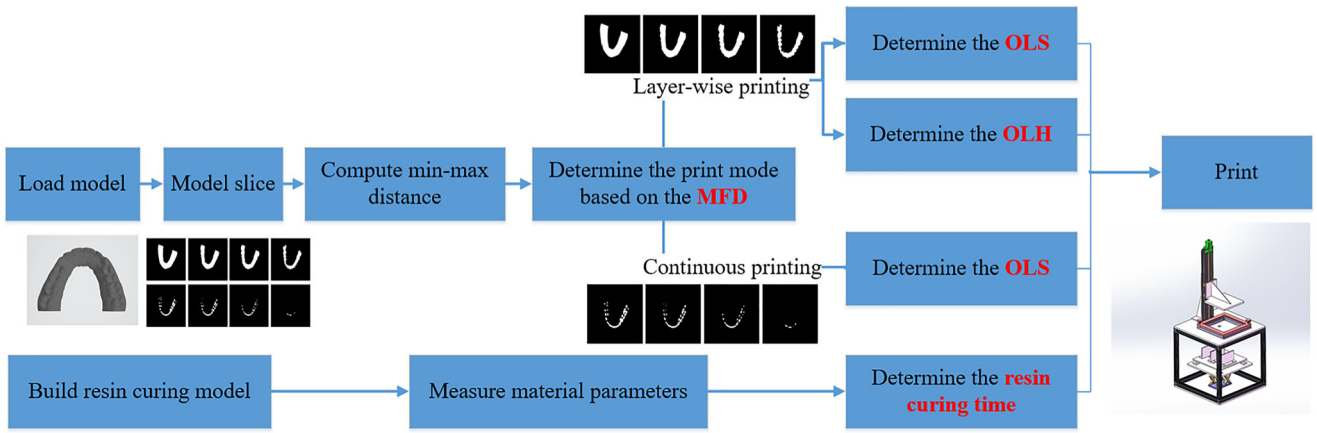

Fig. 3 The optimized control scheme for continuous and layer-wise DLP 3D printing

determined by comparing the min–max distance [16] and MFD. The min–max distance is used to measure the time it takes for resin fill to just fill the currently printed slice. For continuous printing, the OLS of the printing platform is designed as a constant. For layer-wise printing, the OLH and OLS of the printing platform can be estimated through CFD analysis or resin material analysis. The resin curing time might also be estimated in the same way. Figure 3 shows the proposed scheme for combining layer-wise and continuous printing. The estimated control parameters are highlighted in red. The printing time could be shortened for most models based on the optimal printing control parameters.

3 Methods

3.1 Numerical methods

In order to estimate the printing parameters, a numerical model was established, as shown in Fig. 4.

The movement of the printing platform causes perturbation to the fluorinated oil and resin, whose movement was also affected by gravity. The left, right, and bottom boundary of the resin tank are fixed wall. The fluorinated oil and resin are immiscible, and their interface is horizontal initially. The cured part is treated as a moving wall. The initial parameters are defined as follows: H_r is the thickness of the resin, H_f is the thickness of the fluorinated oil, and v_m is the upward speed of the platform lifting. $D_{M-M}[i]$ is the min–max distance for the *i*th slice, and it is computed following the method by Liu et al. [16]. In the numerical simulation, slices of solid structure influence the process reliability more easily than those of hollow structures. So the following assumptions are assigned in the simulation: (1) the viscosity of the resin and fluorinated oil is constant, (2) the cured part is rigid, (3) the cured part and the printing platform are considered as an integrated unity.

In layer-wise and continuous printing, the two-phase interface will show different regimes during the printing process. VOF method [25] is used to capture dynamic changes at the interface of immiscible liquids [26]. The related variables are shown in Table 1. The continuity equation is:

$$\nabla \cdot \boldsymbol{U} = 0 \tag{1}$$

where $\boldsymbol{U}$ is the velocity. The momentum conservation equation is:

$$\frac{\partial (\rho U)}{\partial t} + \nabla \cdot (\rho \boldsymbol{U}\boldsymbol{U}) = -\nabla \mathrm{p} - g \cdot h \nabla \rho + \sigma k \nabla \alpha \tag{2}$$

where $\rho = \alpha_1 \rho_1 + \alpha_2 \rho_2$ is the mixture density of the two-phase. p is the pressure, g is the gravitational acceleration, h is the position vector, σ is the surface stress coefficient, $k = -\nabla \cdot \boldsymbol{n}$ is the interface curvature, and $\boldsymbol{n}$ is the normal vector of the interface.

The volume fraction equation of the resin is:

$$\frac{\partial \alpha_1}{\partial t} + \nabla \cdot (\alpha_1 U) + \nabla \cdot \left(\alpha_1 (1 - \alpha_1) c |U| \frac{\nabla \alpha_1}{|\nabla \alpha_1|} \right) = 0 \tag{3}$$

where α_1 is the volume fraction of resin, $\alpha_2 = 1 - \alpha_1$ is the volume fraction of the fluorinated oil, and c is the interface compression factor.

3.2 Parametric analysis model

During printing, when a layer of resin is cured, the printing platform rises with a gap formed between the printing part and the fluorinated oil. At this time, the resin begins to flow into the gap until the gap is fully filled. Accordingly, a Cartesian coordinate system is established as shown in Fig. 4. It is considered that there is a velocity slip between the resin and the printed object during the movement of the platform. The length of the slip satisfies the linear slip length model [27]. There is no velocity slip between the resin and fluorinated oil, as shown in Fig. 5. Then, the boundary conditions are:

$$u|_{y=H_s} = u_s, u|_{y=0} = 0 \tag{4}$$

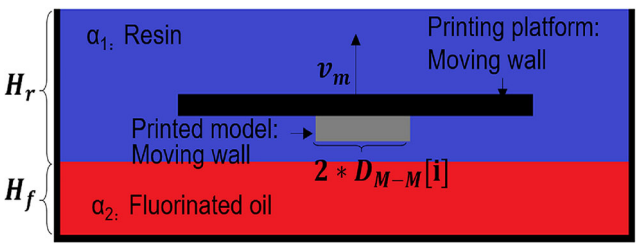

Fig. 4 Geometry of fluorinated oil bed based DLP 3D printing

Table 1 Nomenclature

Symbol	Definition
α_i	Volume fraction of phase *i*
ρ_i	Phase-averaged density, ρ_i (i = 1,2,3) density of phase i
μ_i	Viscosity of phase *i*
$\boldsymbol{U}$	Velocity
p_d	Volume flowrate
$\boldsymbol{g}$	Gravitational acceleration
∇	Gradient operator
C_d	Cure depth
D_p	Transmission depth
E_c	Critical energy for curing
E_o	Cumulative light energy

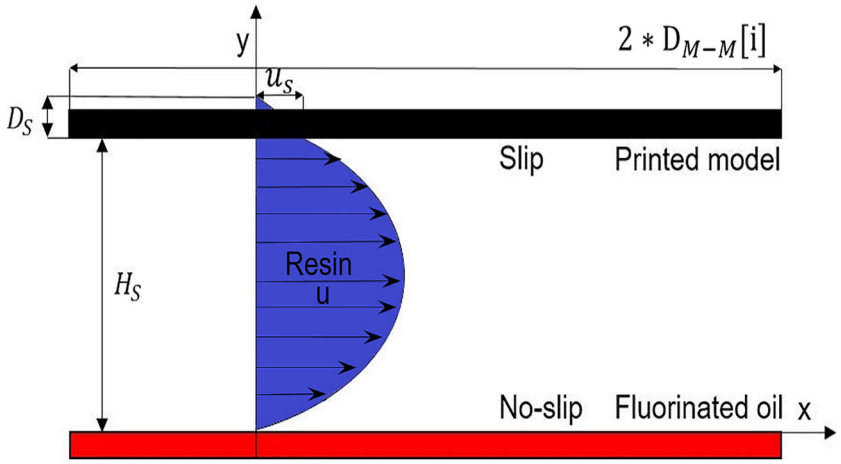

Fig. 5 Schematic diagram of resin flow

where u is the maximum speed of the resin moving along the X-axis, u_s is the slip speed, and H_s is the upward moving height of the printing platform.

The resin flows into the gap between the printed part and the fluorinated oil, and its Reynolds number is less than 1.0 according to the law of laminar flow between the plates. Therefore, it is assumed that the flow in the gap is Poiseuille flow with the simplified N-S equation:

$$\frac{d^2u}{dy^2} = \frac{1}{\mu_1}\frac{dp}{dx} \tag{5}$$

where $^{dp}/_{dx}$ is the pressure gradient. The integral of Eq. 5 has:

$$u = \frac{1}{2\mu_1}\frac{dp}{dx}y^2 + C_1 y + C_2 \tag{6}$$

where C_1 and C_2 are constants. By substituting the boundary condition in Eqs. 4 into 6:

$$C_1 = \frac{u_s}{H_s} - \frac{1}{2\mu_1}\frac{\mathrm{d}p}{dx}H_s \tag{7}$$

$$C_2 = 0 \tag{8}$$

$$u = \frac{1}{2\mu_1}\frac{\mathrm{d}p}{dx}\left(y^2 - H_s \times y\right) + \frac{u_s}{H_s}y \tag{9}$$

According to the assumption of linear slip boundary condition proposed by Navier, the slip velocity is written as:

$$u_s = D_s\frac{du}{dy} \tag{10}$$

where D_s is the slip length. Combining Eqs. 5, 7, and 10, we can obtain:

$$u_s = \frac{1}{2\mu_1}\frac{{H_s}^2 D_s}{H_s - D_s}\frac{dp}{dx} \tag{11}$$

$$u = \frac{1}{2\mu_1}\frac{dp}{dx}\left(y^2 + \frac{2H_sD_s - {H_s}^2}{H_s - D_s}y\right) \tag{12}$$

Therefore, the volume flow Q between the printing part with width W and the fluorinated oil can be expressed as:

$$Q = W\int_0^{H_s} u dy = \frac{W{H_s}^3(4D_s - H_s)}{12\mu_1(H_s - D_s)}\frac{dp}{dx} \tag{13}$$

The average flow rate is:

$$u_{av} = \frac{Q}{WH_s} = \frac{{H_s}^2(4D_s - H_s)}{12\mu_1(H_s - D_s)}\frac{dp}{dx} \tag{14}$$

At time t_1 when the platform rises, there is a relationship between the resin filling distance L_r and the time variable t:

$$\begin{cases} L_r = \int_{t=0}^{t=t_1} \frac{{H_s}^2(4D_s - H_s)}{12\mu_1(H_s - D_s)}\frac{dp}{dx} * t dt \\ H_s = v_m * t \end{cases} \tag{15}$$

where t_1 is the resin filling time for filling distance L_r, which equals to the resin filling time in continuous printing. Layer-wise printing is suitable for printing larger solid slices, so it is challenging to complete the resin filling during the movement of the printing platform for layer-wise printing. After the movement of the printing platform is stopped, the resin filling time from position L_r to position $D_{M-M}[i]$ is represented as t_2:

$$\begin{cases} t_2 = (D_{M-M}\,[\mathrm{i}] - L_r)\,\frac{12\mu_1(H_s - \mathrm{D_s})}{{H_s}^2(H_s - 4\mathrm{D_s})}\left|\frac{dx}{dp}\right| \\ L_r \le D_{M-M}\,[i] \end{cases} \tag{16}$$

Therefore, the resin filling time $T \approx t_1 + t_2$ for layer-wise printing is:

$$\begin{cases} T = \frac{H_s}{v_m} + (D_{M-M}\,[\mathrm{i}] - L_r)\,\frac{12\mu_1}{{H_s}^2}\,\frac{(H_s - D_s)}{(H_s - 4\mathrm{D_s})}\left|\frac{dx}{dp}\right| \\ L_r \le D_{M-M}\,[i] \end{cases} \tag{17}$$

Based on the above equations, resin filling time is affected by platform lifting distance H_s, printing platform lifting speed v_m, the relative ratio of resin and fluorinated oil, and the slices' min–max distances $D_{M-M}[i]$. The relative ratio of resin and fluorinated oil influences the pressure gradient $^{dp}/_{dx}$.

3.3 Resin cure time model

The resin curing time influences the printing quality and efficiency. According to Jacobs' working curve equation [28], a resin curing time model is established:

$$C_d = D_p \cdot \ln\left(\frac{E_o}{E_c}\right) \tag{18}$$

where C_d is the curing depth (μm), i.e., the thickness of a slice. D_p is the transmission depth (μm), and E_o is the light energy (mJ/cm^2) accumulated from the DLP light source at the curing interface (interface between the resin and fluorinated oil). E_c is the critical exposure energy of UV light for resin curing (mJ/cm^2).

In real cases, the intensity distribution of the DLP light source is usually not uniform [29]. Therefore, an illuminance power measurement system was designed to measure the light intensity I (X, Y) at different positions of an exposure plane (X-Y) under different grayscales using a UV energy meter (Newport 1936-R), as shown in Fig. 6. Based on the experimental results, the light intensity E_r (I) of each slice could be obtained by the illumination homogenization algorithm [30], $E_o = E_r\,(I) \cdot t_3$. We assume that the light intensity on the curing interface does not change during the exposure process, so there are:

$$C_d = D_p \cdot \ln\left(\frac{E_r\,(I) \cdot t_3}{E_c}\right) \tag{19}$$

Therefore, for slices with different layer thicknesses, the curing time t_3 can be expressed as:

$$t_3 = \frac{E_c \cdot e^{\frac{C_d}{D_p}}}{E_r\,(I)} \tag{20}$$

According to Eq. 20, the corresponding relationship between layer thickness and curing time can be obtained in the process of layer-wise printing. However, the continuous printing platform is lifted continuously, and the light intensity from the DLP projector to the curing volume decreases as increase of the curing depth. Therefore, it is necessary to explore the relationship between the speed and the curing depth to ensure the curing of the slices. According to the Beer-Lambert law [11]:

$$P\,(z) = P_0 \cdot e^{-z/D_p} \tag{21}$$

where $P\,(z)$ is the illuminance power (mW/cm^2) at a certain depth z (μm) away from the printing interface. In the meantime, $z\,(t) = \mathrm{v}_m \cdot t$. In addition, for the slice at z, the critical curing energy E_c is:

$$E_c = \int_t^0 P\,(z)\,dt = \frac{E_r\,(I) \cdot D_p}{v_m}\left(1 - e^{-v_m \cdot t/D_p}\right) \tag{22}$$

Under the presupposition of guaranteeing curability, the relationship between the continuous printing platform rising speed v_m and the maximum curable thickness z is:

$$z = -D_p \cdot \ln\left(1 - \frac{E_c \cdot v_m}{E_r\,(I) \cdot D_p}\right) \tag{23}$$

4 Simulation and verification

To simulate the influence of the platform lifting distance, printing platform lifting speed, the relative ratio of resin and fluorinated oil, and the slices' min–max distances on the resin filling time, some default parameters were set. The gravity acceleration is 9.8 m/s^2, and the density and viscosity of the fluorinated oil are 1390 kg/m^3 and 0.012 Pa.s, respectively. The density and viscosity of the resin density are 1120 kg/m^3 and 0.224 Pa.s, respectively. Figure 7 shows the initial scene in simulations established by OpenFOAM according to the above parameters, in which the relative volume ratio of fluorinated oil to resin was 1:5.

The system in Fig. 8a is designed to verify the simulation results. The actual setup is shown in Fig. 8b. The DLP light source (BenQ TK800M) is under the resin tank. A Tucson MT-500 camera, an MZ1000 monocular microscope, and a ZT-301 cold light source were used to capture the resin filling process in real time.

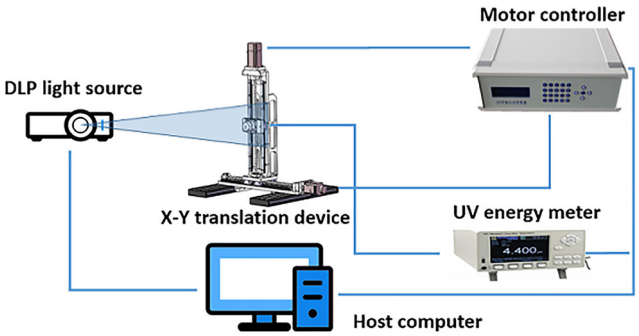

Fig. 6 Illuminance power measurement system

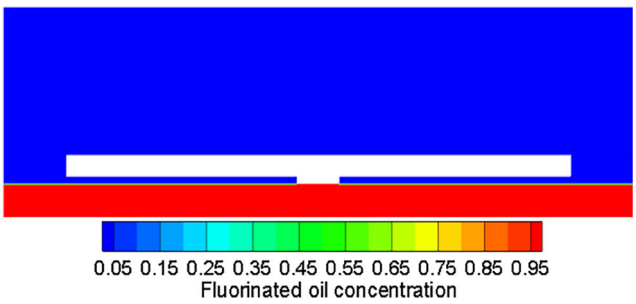

Fig. 7 Contour of volume fraction of the fluorinated oil at the initial condition

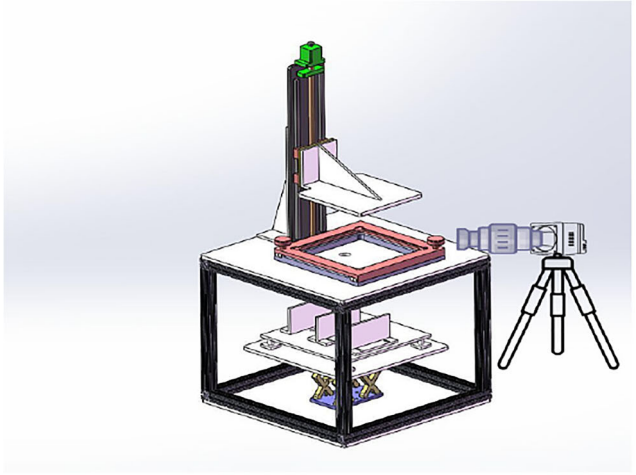

(a)

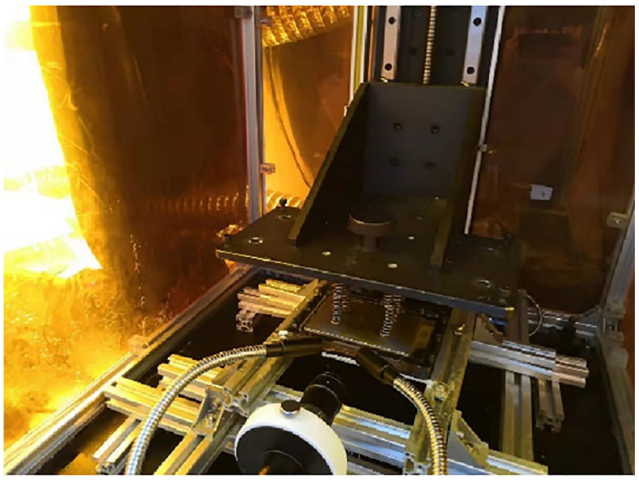

(b)

Fig. 8 Experimental verification equipment. **a** The hardware design of simulation results verification. **b** A practical device

4.1 Influence of printing platform lifting distance on filling time

As shown in Fig. 9, the lifting distance H_s of the printing platform was set as 1 mm, 2 mm, 3 mm, 4 mm, or 5 mm, respectively. The $D_{M-M}[i]$ of the slices was 7.5 mm. The lifting speed v_m of the platform was 15 mm/s. And the depth ratio of fluorinated oil to resin was 1:5. It can be seen from Fig. 9a–f that the higher the H_s, the more quickly the resin flows. In the best cases, the gaps between interface of the resin and fluorinated oil will be completely filled up in 0.5 s after printing a single layer.

The simulations in Fig. 9b–d are verified by experiments, as shown in Fig. 10a–c.

By comparing Figs. 9 and 10, it can be concluded that the actual printing results generally match simulations. On the other hand, the full time of simulation filling is slightly slower than the actual. The reason is that the classical VOF model is used to simulate the two phases' flow, and potential slip motions between the two phases have not been considered. That is to say, the proposed model is a simplified approximation of the actual situation and the simulated resin filling time is generally longer than that in real cases. But the simulated resin filling time is longer than that in the practical scenes because it does not consider the slip motion. Therefore, the filling time obtained from simulations can be used as a lower limit to estimate the resin filling time in practical printing tasks.

4.2 Influence of printing platform lifting speed on filling time

When the lifting distance is set as an invariant, the increase of the printing platform's lifting speed v_m will reduce the lifting time. The fast lifting is helpful for resin filling, thereby reducing printing time. To demonstrate this, the lifting distance was assigned as 2 mm, and $D_{M-M}[i]$ was 7.5 mm. At the same time, the lifting speed v_m was assigned as 5 mm/s, 10 mm/s, 15 mm/s, 20 mm/s, and 25 mm/s, respectively. The corresponding simulations are shown in Fig. 11a–e. Figure 11f demonstrates that the distance of resin filling increases with the increase of v_m. It can be observed that the increase of the printing platform's rising speed is beneficial to the resin refilling.

Figure 12a to c are the resin filling distances in real using the same parameters as in simulations (Fig. 11a–c).

4.3 Influence of the fluorinated oil to resin ratio on filling time

As shown in Eq. 17, increasing the resin height H_r will increase the driving force of the resin movement and accelerate the resin flow. In Fig. 13a–e, $D_{M-M}[i]$ was 7.5 mm, v_m was 15 mm/s, the lifting distance was 2 mm, and the ratio of fluorinated oil to resin was 1:3, 1:4, 1:5, 1:6, and 1:7 respectively. Figure 13f demonstrates that increasing the relative portion of resin can reduce the resin filling time. However, compared with the driving force $\rho_1 g H_r$, the height of the resin H_r has less influence.

4.4 Influence of slices' min–max distances on filling time

To explore the influence of different slices' min–max distances $D_{M-M}[i]$ on the resin filling speed, v_m was fixed at 5 mm/s, and H_s was set as 2 mm. The $D_{M-M}[i]$ in different models were 1 mm, 2 mm, 4 mm, 7.5 mm, and 10 mm. The corresponding resin filling distance is shown in Fig. 14a–e. It can be seen that lifting the platform will result in a more significant fluctuation on the free-surface with the

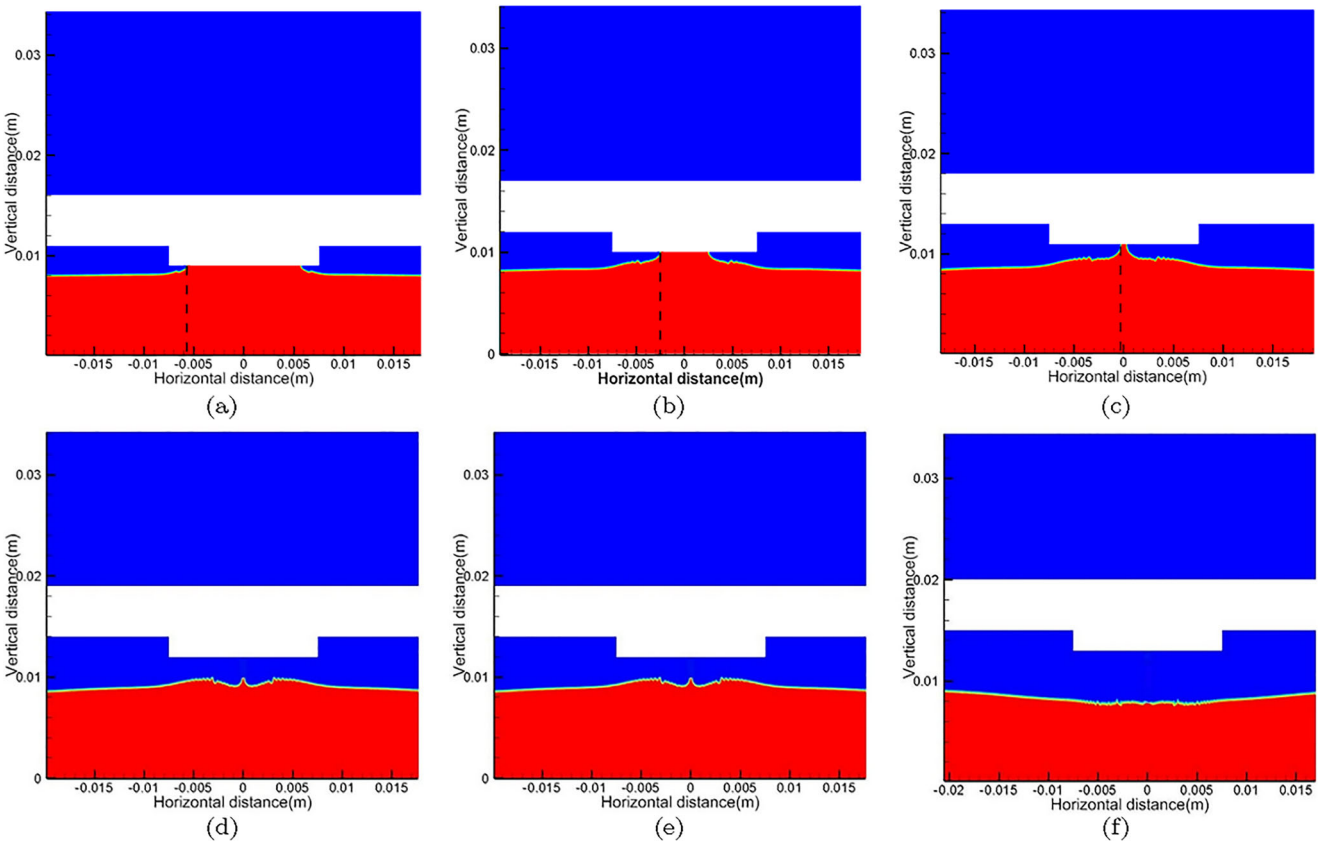

Fig. 9 Influence of printing platform lifting distance on resin filling distance. **a** H_s=1 mm. **b** H_s=2 mm. **c** H_s=3 mm. **d** H_s=4 mm. **e** H_s=5 mm. **f** The relationship between the lifting distance of the printing platform and the resin filling distance

increase of $D_{M-M}[i]$ the resin. Figure 14f shows that T is a quadratic function of $D_{M-M}[i]$ because dx in Eq. 17 is proportional to $D_{M-M}[i]$.

Figure 15a to c are the experimental verifications of Fig. 14c–e. It can be observed that the actual printing process is very similar to the simulations. Therefore, an increase of the $D_{M-M}[i]$ of the slice will affect the filling time T of resin.

5 Estimation of key printing control parameters

The key parameters in our printing scheme are the resin curing time, MFD for continuous printing, OLH for layer-wise printing, and OLS for continuous and layer-wise printing. This section shows how to estimate these parameters.

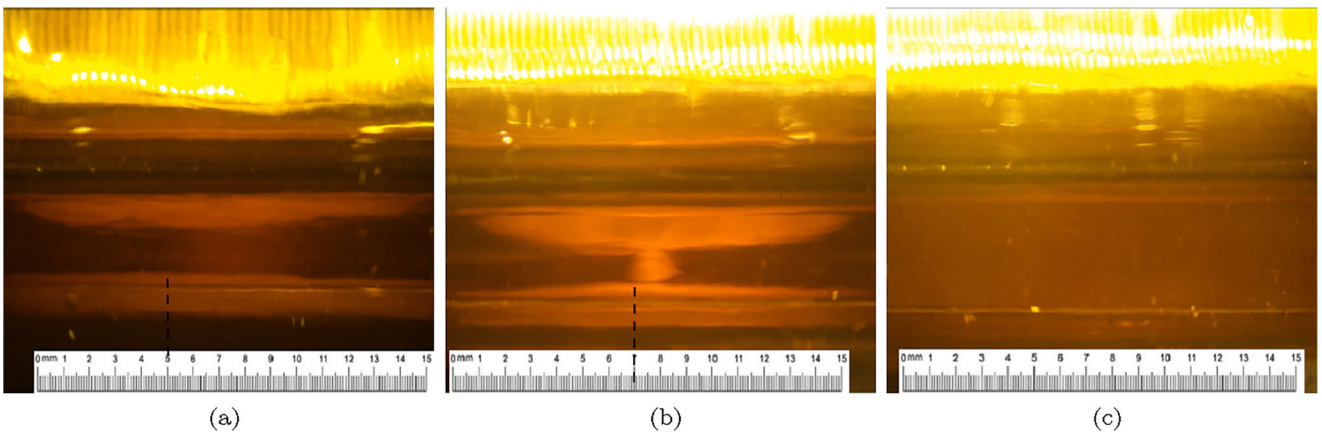

Fig. 10 Verification of simulations in Fig. 9. **a** Printing platform lifting 2 mm and resin filling 0.5 s. **b** Printing platform lifting 3 mm and resin filling 0.5 s. **c** Printing platform lifting 4 mm and resin filling 0.5 s

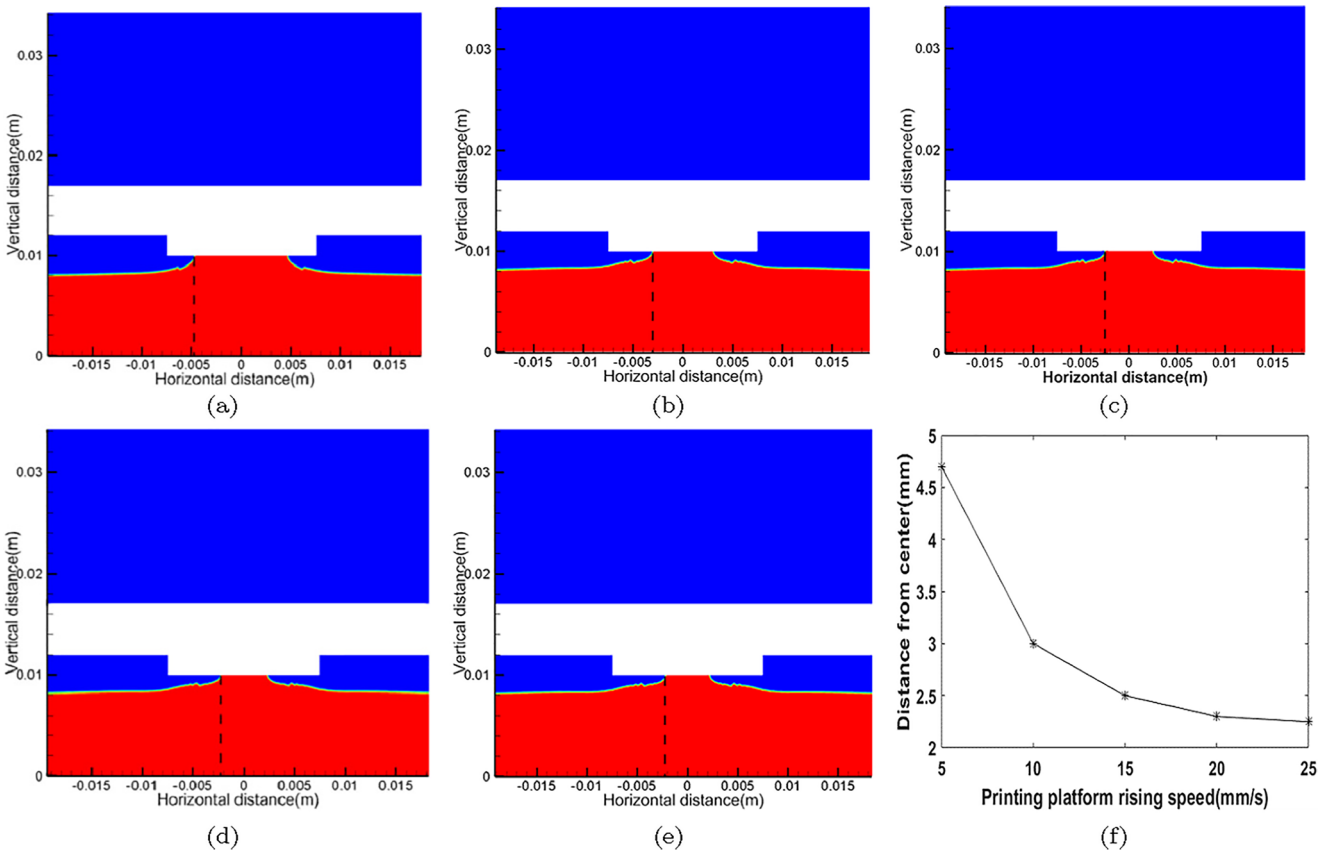

Fig. 11 Influence of printing platform rising speed on resin filling distance. **a** v_m=5 mm/s. **b** v_m=10 mm/s. **c** v_m=15 mm/s. **d** v_m=20 mm/s. **e** v_m=25 mm/s. **f** The relationship between the printing platform rising speed and the resin filling distance

5.1 Estimation of resin curing time

The transmission depth D_p and the critical exposure E_c of the photosensitive resin determine the curing level required for each layer of resin in the layer-wise and continuous printing process, as shown in Eqs. 18 and 23. The equipment setup in Fig. 16 is employed to verify these two equations. The DLP light source was located above the resin tank, and the distance from the DLP light source to the interface of resin and fluorinated oil. A Newport 1936-R power meter was used to measure the light intensity after homogenization, which was 7.5 (mW/cm^2). The resin was irradiated for 5, 10, 15, 20, and 25 s, respectively. The curing depth C_d and cumulative light energy $\ln(E_o)$ at different exposure times are recorded as shown in Table 2. The curve fitting result is shown in

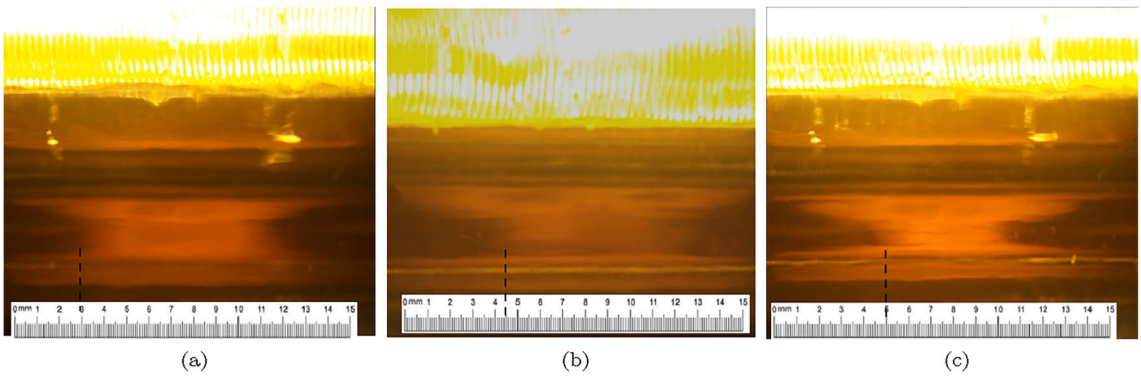

Fig. 12 Verification of simulations in Fig. 11. **a** Printing platform rising 5 mm/s and resin filling 0.5 s. **b** Printing platform rising 10 mm/s and resin filling 0.5 s. **c** Printing platform rising 15 mm/s and resin filling 0.5 s

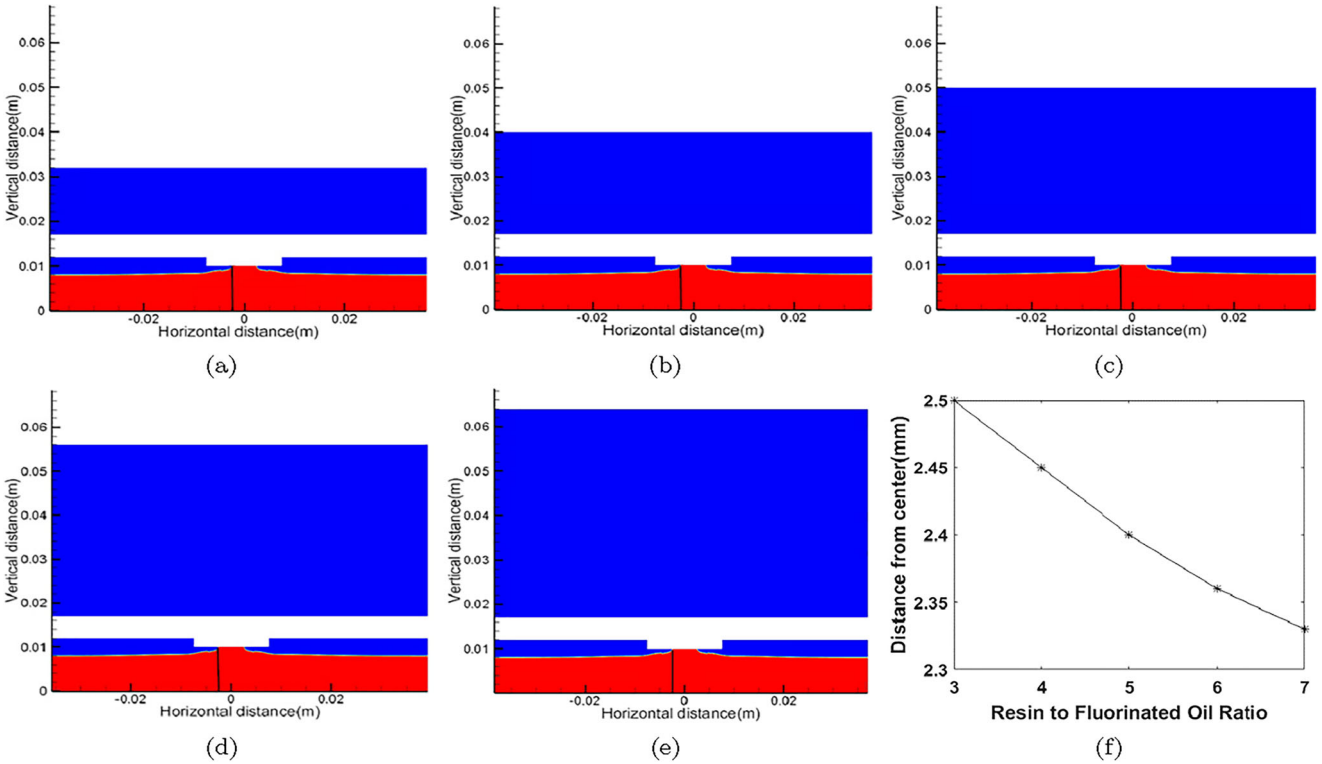

Fig. 13 The effect of resin to fluorinated oil ratio on resin filling distance. **a** $H_f : H_r = 1 : 3$. **b** $H_f : H_r = 1 : 4$. **c** $H_f : H_r = 1 : 5$. **d** $H_f : H_r = 1 : 6$. **e** $H_f : H_r = 1 : 7$. **f** The relationship between the resin to fluorinated oil ratio and the resin filling distance

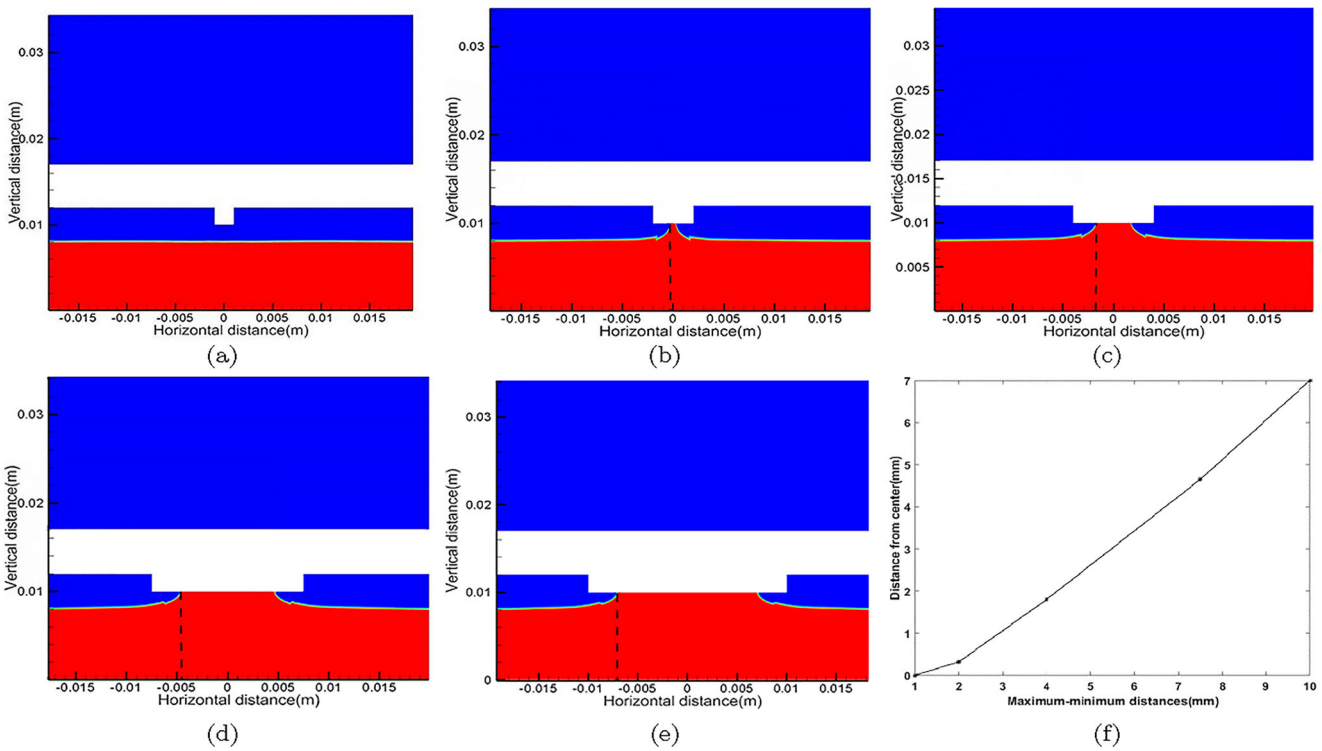

Fig. 14 Influence of min-max distances on resin filling. **a** D_{M-M} [i]=1 mm. **b** D_{M-M} [i]=2 mm. **c** D_{M-M} [i]=4 mm. **d** D_{M-M} [i]=7.5 mm. **e** D_{M-M} [i]=10 mm. **f** The relationship between the min–max distance and the resin filling distance

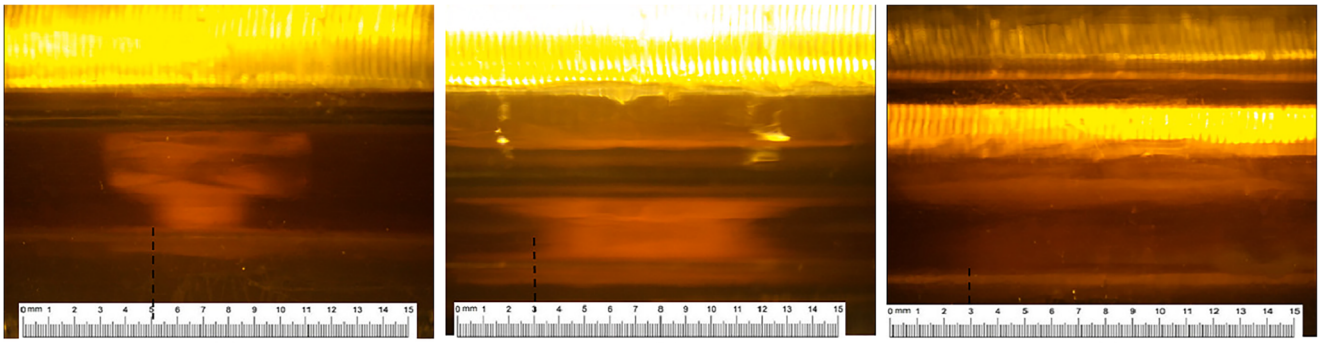

Fig. 15 Verification of simulations in Fig. 14. **a** D_{M-M} [i]=4 mm and resin filling 0.5 s. **b** D_{M-M} [i]=7.5 mm and resin filling 0.5 s. **c** D_{M-M} [i]=10 mm and resin filling 0.5 s

Fig. 17, which is consistent with the theoretical analysis. According to Eq. 18, the penetration depth of the light used in the experiment is D_p=0.74 mm, and the critical exposure E_c is 18 (mJ/cm^2). According to Eq. 19, if the thickness of the printed slice is 0.1 mm, the required curing time in layer-wise printing is 2.8 s. This has been verified in real printing trials, in which the curing time was measured to be 3 s.

5.2 Estimation of MFD

For continuous printing, the resin needs to fill the gap between the printing platform and the upper surface of the fluorinated oil as the platform is being lifted. At the same time, the resin filled in the gap should be fully cured before the next frame of the image is played. So for continuous printing, the largest D_{M-M} [i] in all slices needs to be less than or equal to MFD, the combination Eq. 15 has:

$$\begin{cases} \mathrm{MFD} = u_{av} * t = \int_{t=0}^{t=1/\mathrm{f}_n} \frac{{H_s}^2(4D_s - H_s)}{12\mu_1(H_s - D_s)} \frac{dp}{dx} * tdt \\ H_s = v_m * 1/\mathrm{f}_n \end{cases} \tag{24}$$

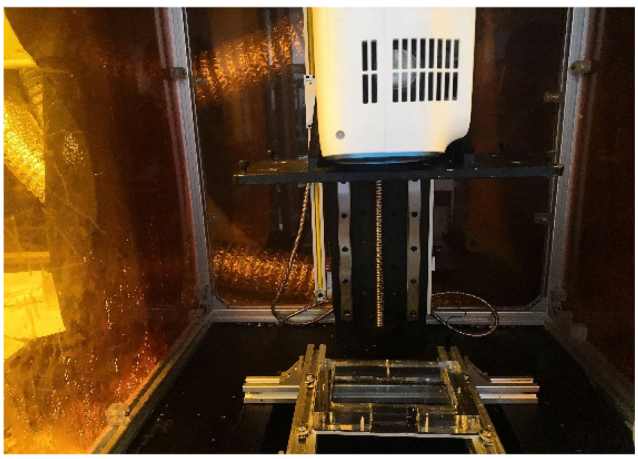

Fig. 16 Measuring device for transmission depth and critical exposure

Then it can be deducted that:

$$\mathrm{MFD} = \frac{{v_m}^2}{{f_n}^4} \cdot \frac{1}{C_3} \cdot \frac{1}{24\mu_1} |\frac{dp}{dx}| \tag{25}$$

The v_m in the equation needs to meet the requirements of the curing depth of the conditional continuous printing resin single layer. But the slip distance D_s associated with C_3, and the pressure gradient $|\frac{dp}{dx}|$ in Eq. 25 is unknown. So we estimated MFD according to numerical simulation results. $|\frac{dp}{dx}|$ represents the pressure gradient between the boundary of the model and the boundary of the current filling position when the resin is filled. And the resin and fluorinated oil are incompressible fluids. Therefore, the lifting speed was 5 mm/s, the lifting distance was 4mm, and D_{M-M} [i] was 7.5 mm. The cross-sectional distribution of $^{dp}/_{\rho_1}$ at the filling area is shown in Fig. 18 after the platform has been lifted for 0.6 s. A $|\frac{dp}{dx}| = 8.07 * 10^5$Pa/m can be deducted. We calculate the pressure gradient of different lifting speeds, lifting distances, and the maximum diameter of the printed model slices, and find that the difference between it and $8.07 * 10^5$Pa/m is less than 3%. Therefore, it is considered that $|\frac{dp}{dx}|$ is approximately a constant of $8.07 * 10^5$Pa/m.

The lifting speed of the continuous printing platform is slow, and it can be considered that there is a very small slippage between the resin and the printing platform:

$$\mathrm{MFD} \approx \frac{{v_m}^2}{{f_n}^4} \cdot \frac{8.07 * 10^5}{24\mu_1} \tag{26}$$

Let us assume that the DLP light source switches 1 slice image per second, and the rising speed of the printing platform is 0.1 mm/s. At this time, according to Eq. 26, the MFD is 1.5 mm. Figure 19 shows the actual printing test based on the above parameters. From left to right are the printed cuboids, whose heights are all 10 mm, while their cross-sectional areas are 2 mm*2 mm, 3 mm*3 mm, 3.5 mm*3.5 mm, 4 mm*4 mm, and 4.5 mm*4.5 mm corresponding to MFD 1 mm, 1.5 mm, 1.75 mm, 2 mm, and 2.25 mm. It can be seen that the 2 mm* 2 mm and 3 mm*3

Table 2 Cure depth at different exposure energies

Cumulative light intensity (mw/cm^2)	37.5	75	112.5	150	187.5
Filling time (s)	0.6	1	1.2	1.6	1.8

mm cuboids have smoother surfaces, while the surfaces of 3.5 mm*3.5 mm, 4 mm*4 mm, and 4.5 mm*4.5 mm cuboids are rougher. There are dents of different sizes resulting from insufficient resin filling, so the MFD estimated by simulation is consistent with that in the practical printing.

5.3 Estimation of OLH

According to the simulation results in Fig. 9f, the layer-wise printing has an OLH. Therefore, Eq. 17 can be simplified into Eq. 24 to obtain the OLH:

$$T \approx \frac{H_s}{v_m} + L_m \frac{6\mu_1}{{H_s}^2} C_3 \left|\frac{dx}{dp}\right| - \frac{{H_s}^2}{4{v_m}^2} \tag{27}$$

where the slip length D_s is much smaller than the lifting height H_s of the printing platform, and $(H_s - D_s) / (H_s - 4\mathrm{D}_s)$ in Eq. 17 is can be taken as a constant C_3, which is greater than 1. According to Eq. 27, it can be observed that when the lifting distance of the printing platform is higher than a certain value, it has almost no effect on the resin filling time, and the H_s is assigned as OLH. In addition, Fig. 20 also proves that different D_{M-M} [i]s have their corresponding OLHs.

To verify the accuracy of the simulations and the expression of the relationship between OLH and filling time in Eq. 27, D_{M-M} [i] of 2 mm, 4 mm, 7.5 mm, and 10 mm were tested in real printed experiments. The printed samples are shown in Fig. 21. It can be seen that models with side lengths of 4 mm and 8 mm have OLH less than or equal to 3 mm. OLH for the mode of side length of 15 mm is 4 mm, and 5 mm for the model of side length of 20 mm. The results are consistent with simulations in Fig. 20.

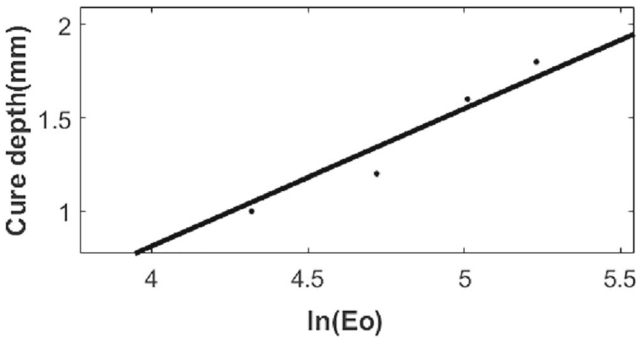

Fig. 17 Fitting results of exposure energy and curing depth

5.4 Estimation of OLS

When the lifting speed exceeds a certain value, the flowing distance of the resin will reach a plateau, as shown in Fig. 11f. In the meantime, if the lifting speed is too fast, it may bring other problems. Therefore, it is necessary to find the optimum lifting speed by considering the OLS of the two printing modes separately.

5.4.1 OLS for continuous printing

In continuous printing, the printing platform is lifted continuously. In the meantime, the resin filling the gap between the printed part and the fluorinated oil should be fully cured to ensure the quality of the printed product. Therefore, Eq. 23 needs to be satisfied. However, this is affected by the mechanical accuracy, image updating speed, resin curing speed, and data transmission speed. The lifting speed of continuous printing cannot be infinite. Taking the TBI screw at the C5 level, for example, the mechanical precision is 10 um, and the minimum thickness of the slice is 10 um. Therefore, for continuous printing, the minimum value of the rising speed is 10um/s. If we print n slices per second, then the minimum lift speed is n*10um/s.

Let us assign the mechanical precision as ε and the number of frames updated per second as f_n. We can obtain the lifting speed of the printing platform in continuous printing:

$$\varepsilon \cdot f_n \le v_m \le \frac{E_r\,(I) \cdot D_p}{E_c} \tag{28}$$

For our system, if we need to print with an accuracy of 20 um per layer and f_n is three, the OLS for our system in continuous printing is 60 um/s.

5.4.2 OLS for layer-wise printing

Both layer-wise and continuous printing require the resin to be quickly refilled. However, layer-wise printing is different from continuous printing as the light projection is separated

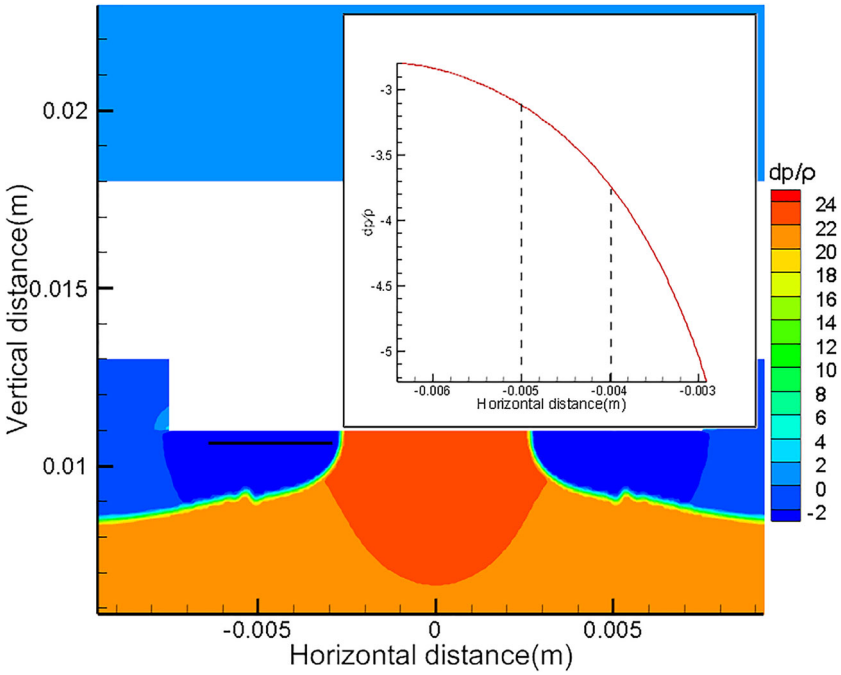

Fig. 18 Pressure gradient distribution

by dark intervals. Therefore, the image updating speeds need to be considered. Furthermore, if the rising speed of printing platform is too fast, it is possible to induce significant fluctuations to the interface between the resin and the fluorinated oil. Therefore, the layer-wise printing speed needs to be determined according to the lifting height of the printing platform, the mechanical system, and the stability of the interface between the two-phase flows.

The printing platform, the printing object, and the connection device between the platform and the lead screw are considered as the load of the mechanical system. As the weight of the load increases, the torque of the motor will increase, and the speed of the motor will decrease. It will limit the rising speed of the printing platform. Taking the J-5718HB3401 type motor equipped with a C5 grade TBI fine lead screw with a precision of 10 um as an example, its lead is 5 mm, and the load is 8 kg. To ensure the stability of the entire system operation, the fastest rising speed of the printing platform is 30 mm/s.

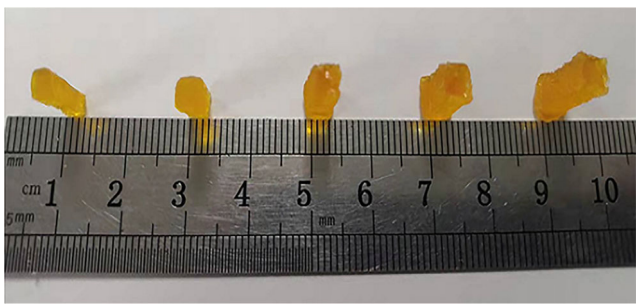

Fig. 19 MFD print verification

The rise of the printing platform lifts the printed parts from the interface, resulting in the interface's interfacial wave between the resin and the fluorinated oil in the form of a hyperbolic sine decreasingly from the center to the periphery. We simulated that the printing platform with the printed part of $D_{M-M}[i]$ of 7.5 mm was lifted by 5 mm at speeds v_m of 5 mm/s, 10 mm/s, 15 mm/s, 20 mm/s, 25 mm/s, and 30 mm/s respectively, as shown in Fig. 22. It can be seen that the interface fluctuation is minimal when $v_m \leq 15$ mm/s. When v_m is greater than 20 mm/s, there is a significant fluctuation at the interface. It is necessary to wait until the interface is stable before printing the next layer, which undoubtedly increases the printing time. Furthermore, we plotted the fluctuation variation of the two-phase interface in the range of 0–0.6s with speeds v_m of 5 mm/s, 15 mm/s, and 30 mm/s respectively as shown in Fig. 23. It can be seen that when v_m=15 mm/s, the free-surface tends to be stable after the resin is filled, and when v_m=30 mm/s, the free-surface oscillates due to the interfacial wave. Therefore, we take v_m=15 mm/s as OLS for layer-wise printing.

6 Experiments

Based on the printing control scheme, the system in Fig. 8b is used for printing. To ensure that the model sticks to the board, the first three layers of all models were printed in the

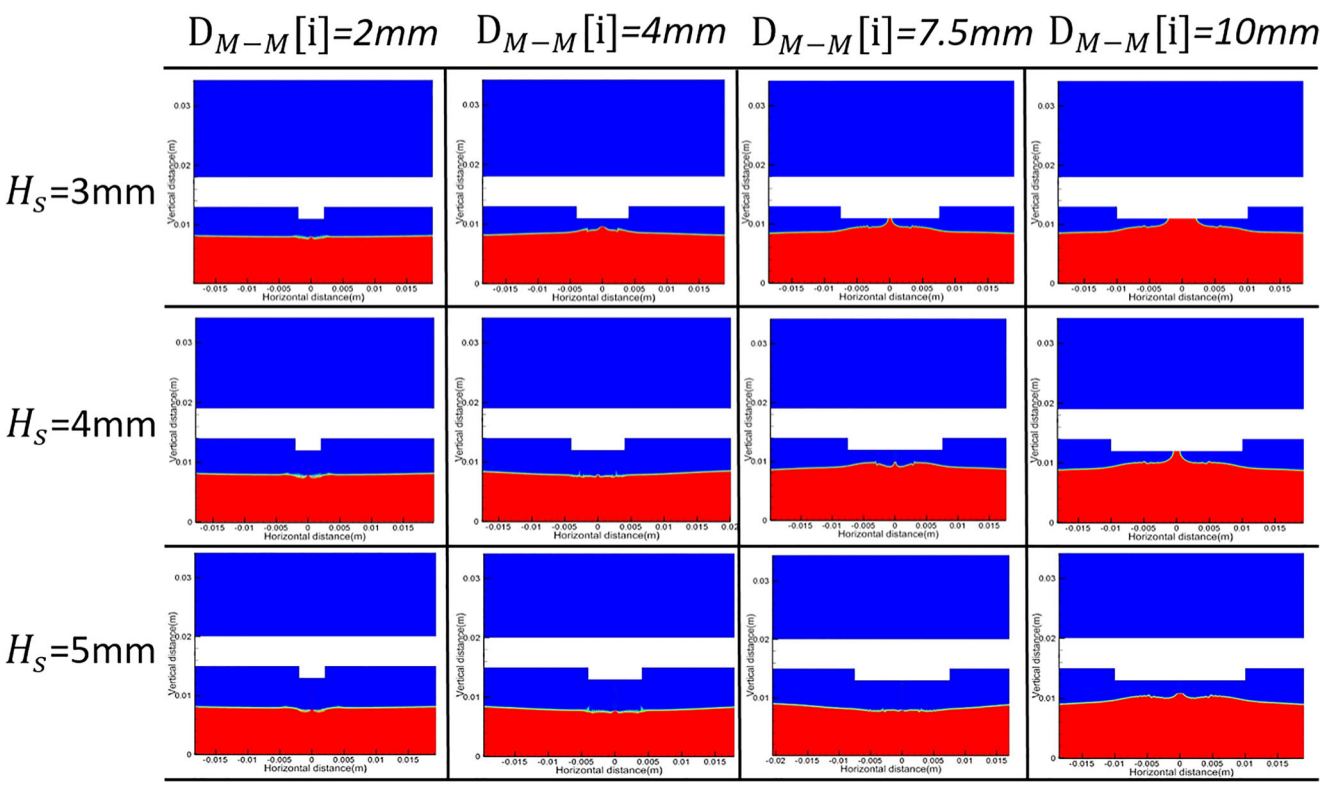

Fig. 20 Simulation of different D_{M-M} [i]s corresponding to OLH

layer-wise printing mode. The exposure time was 12 s, and the dark time was 4 s. To ensure the stability of the free-surface, the printing platform descended at the same speed as it ascends. Figure 24a is a teeth model to be printed, and Fig. 24b is the largest model printed in continuous mode. In the continuous mode, we used the same parameters as Li's method [17], i.e., a lifting speed of 60 μm/s, and an image updating time of 1.6 s. Accordingly, the calculated MFD for the slice is 3.6 mm. Increasing the model's size under the same settings resulted in failures because the resin cannot get refilled completely, as shown in Fig. 24c. Although the model in Fig. 24a can be printed continuously in the vertical direction, it requires additional support and post-processing, which undoubtedly increases printing time and material cost. Using our proposed method, the model was firstly analyzed and processed according to the size of an adult's teeth. The selection of continuous printing or layer-wise printing for the current slice layer of the model

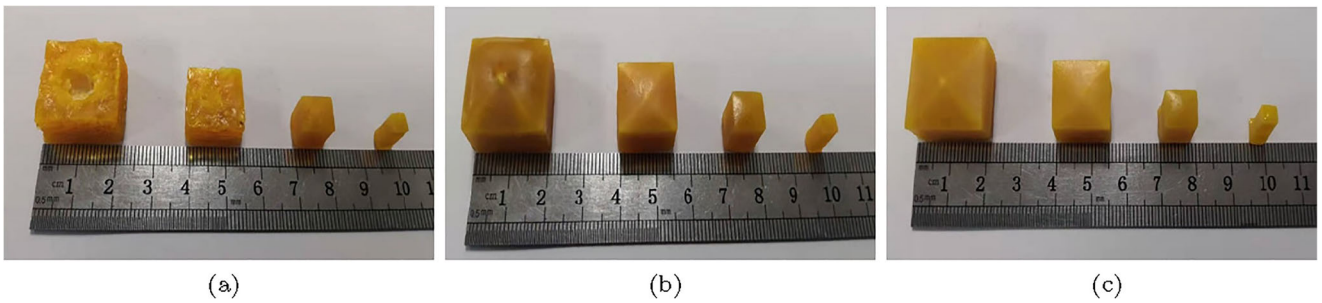

Fig. 21 Print test of different D_{M-M} [i]s corresponding to different lifting heights. **a** Lifting height 3 mm. **b** Lifting height 4 mm. **c** Lifting height 5 mm

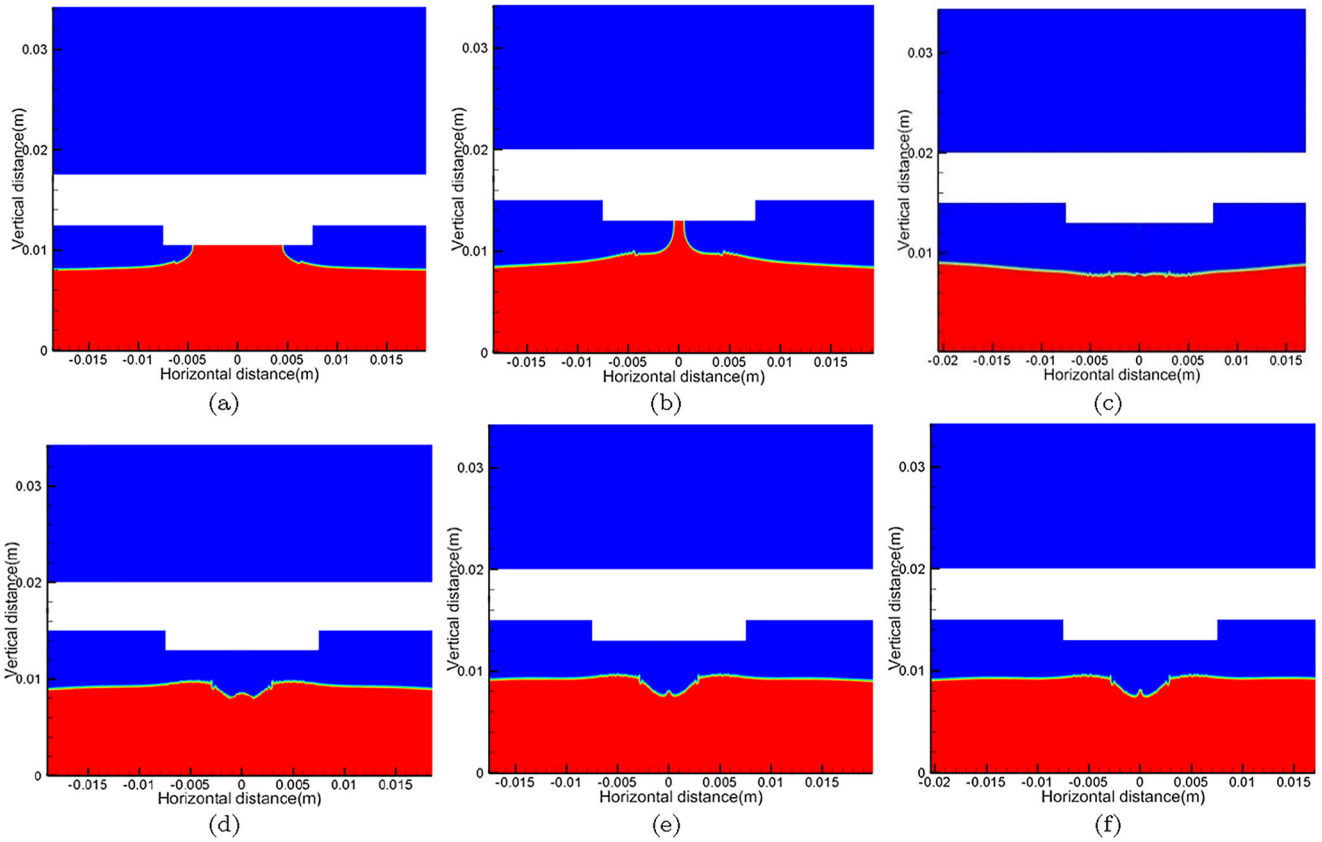

Fig. 22 Effects of different lifting speeds on free-surface stability. **a** v_m=5 mm/s. **b** v_m=10 mm/s. **c** v_m= 15 mm/s. **d** v_m= 20 mm/s. **e** v_m= 25 mm/s. **f** v_m= 30 mm/s

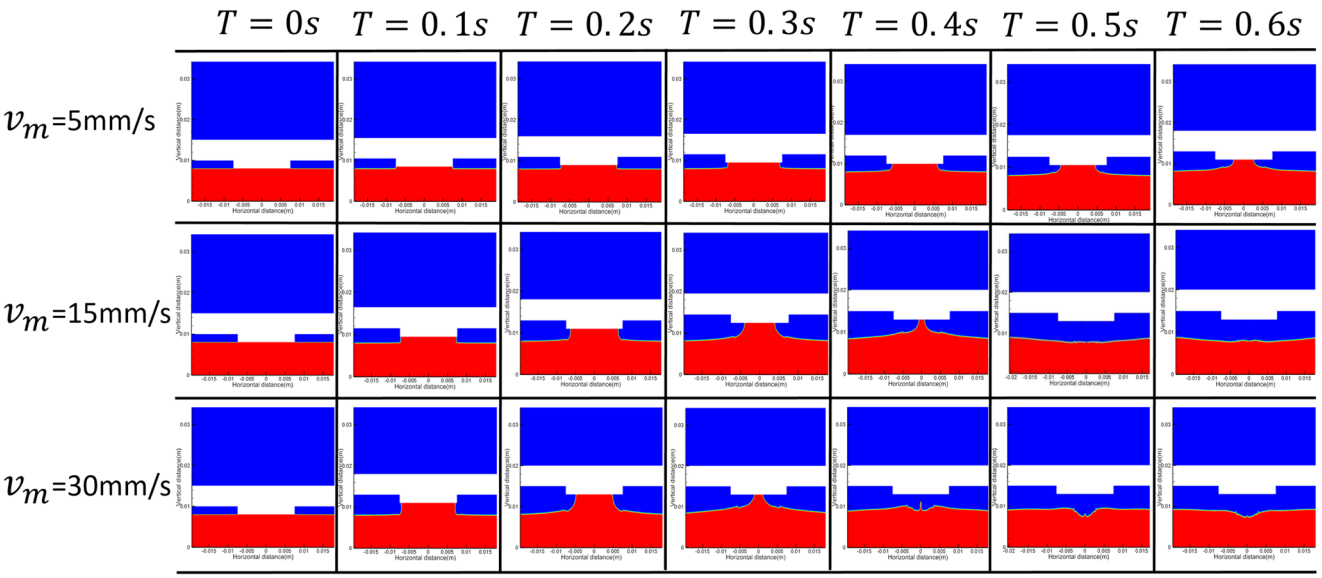

Fig. 23 Effects of different lifting speeds on free-surface stability

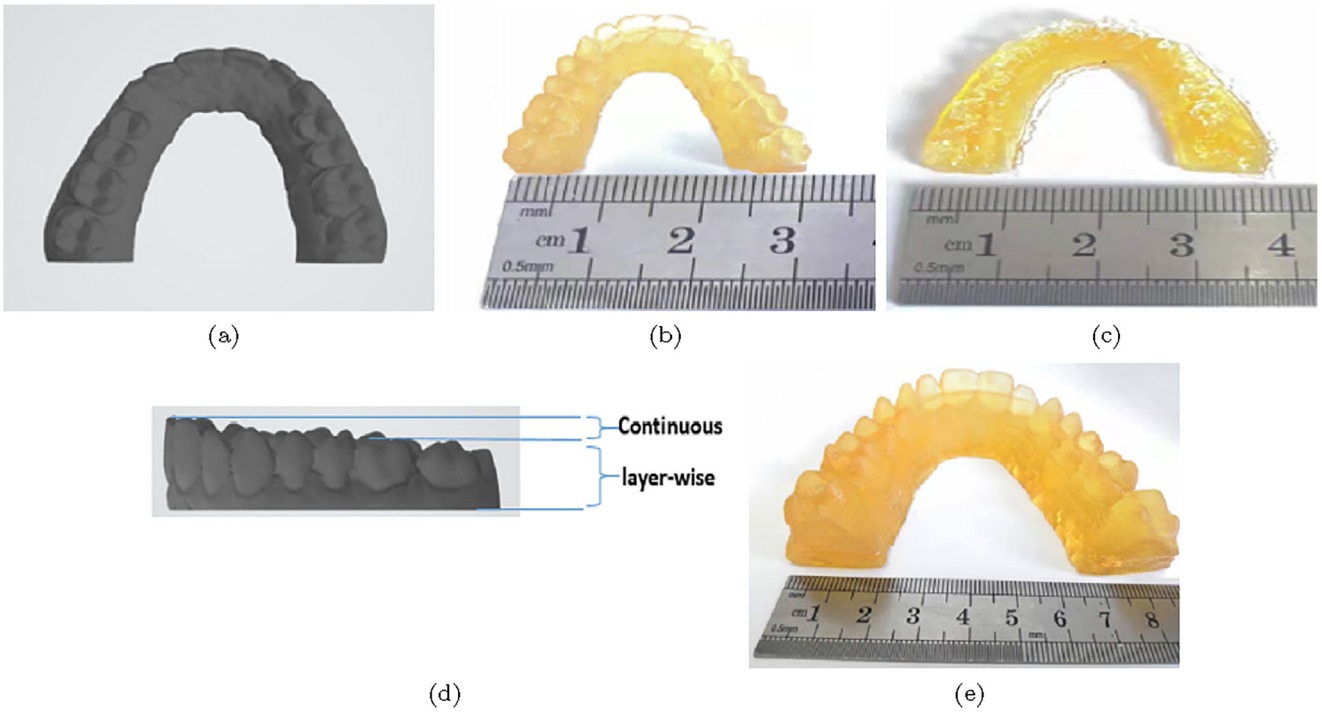

Fig. 24 Comparison of products with continuous printing. **a** Teeth model. **b** The largest model printed in continuous mode. **c** Increase the size of the model under the same settings as **b**. **d** The selection of continuous printing or layer-wise printing for the current slice layer. **e** The actual print model according to the size of an adult's teeth

is marked in Fig. 24d, and e is the actual print model. The proposed method can print solid structures, which cannot be printed using continuous printing. Figure 25a is a child femur model. Most slices of the model are solid and its $D_{M-M}[i]$ are larger than the MFD, so it cannot be printed continuously. The printed model is shown in Fig. 25b. The printing times of Fig. 24e and b are shown in Table 3.

In order to verify the effectiveness of the proposed method, the model in Li's method [17] was printed. The actual printing result is shown in Fig. 26. The printing

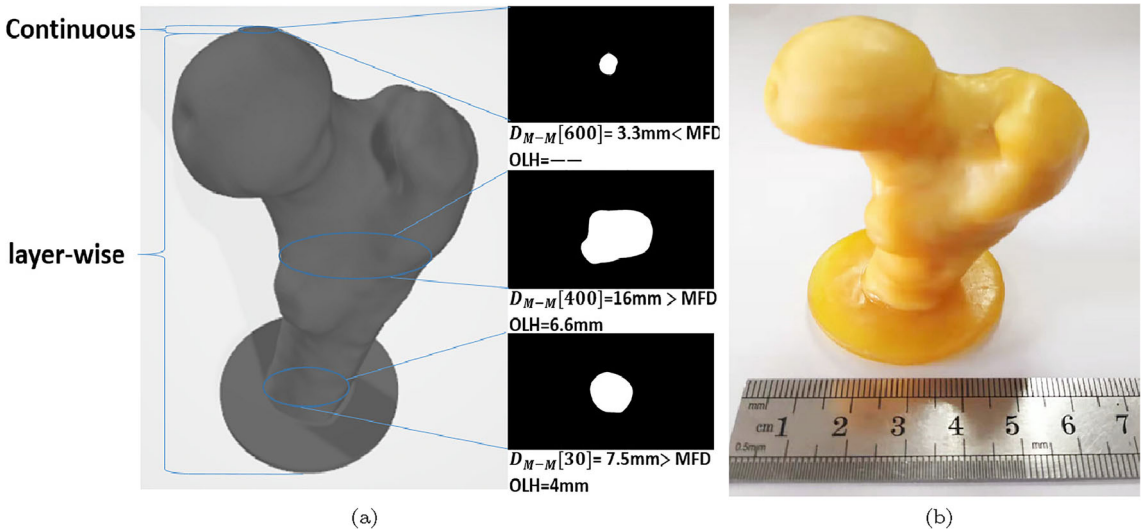

Fig. 25 Femur model with more solid slices. **a** The child femur model. **b** Normal scale print model

Table 3 The print time for models

Model	Teeth	Femur	Tower	Gear
Layers	67	610	491	72
Printing time (s)	320	2750	1320	228
Li's method	–	–	3120	–

time is shown in Table 3. It can be seen that our method requires less time for the same models. The key is the accurate printing control parameters optimized by numerical simulation.

7 Conclusions

In this paper, a CFD-based 3D printing control scheme is proposed to optimize the printing control parameters and overcome the insufficient compatibility of continuous printing with solid structures and limitations of experiment-based optimization of control parameters when using a fluid low adhesion interface. The main idea is to use the VOF method to establish a numerical model to simulate the variation of the free-surface between the resin and the fluorinated oil after printing. Furthermore, based on Poiseuille flow, Jacobs working curve, and Beer-Lambert law, the relationship between the key printing parameters is determined. According to the established relationship and numerical model, the key parameters include resin curing time, MFD for continuous printing, OLH for layer-wise printing, and OLS of the printing platform for both continuous and layer-wise printing can be estimated. The experimental results show that the numerical model established in this paper can well approximate the practical printing situation. The optimal printing control parameters such as MFD and OLH from simulations are in consistent with those found in the actual printing. The printing time for a given model required in our method is much shorter than those needed by other existing methods. The practical printed models demonstrate that the proposed method can print larger-scale models with solid structures and take less time.

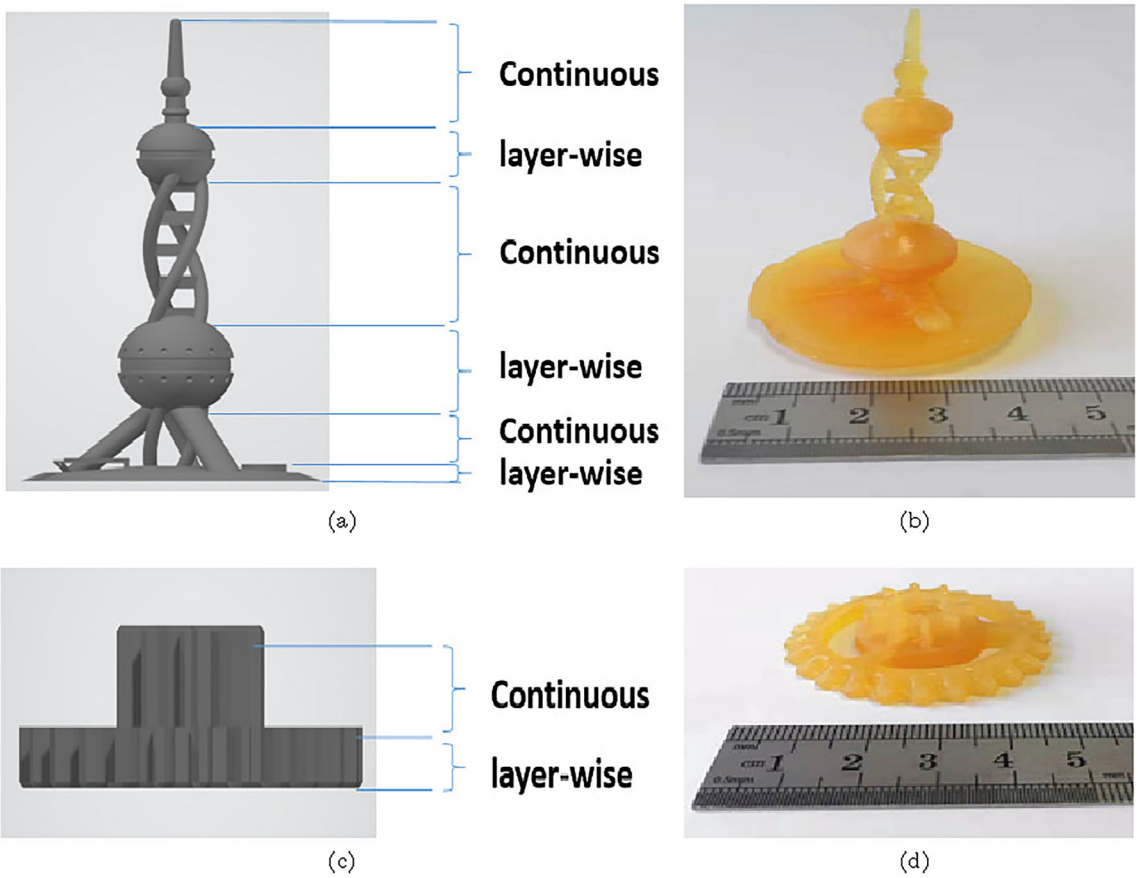

Fig. 26 3D models to be printed. **a** Tower model. **b** Printed tower model. **c** Gear model. **d** Printed gear model

Supplementary Information The online version contains supplementary material available at https://doi.org/10.1007/s00170-022-10658-6.

Supplementary information Movie S1. Numerical simulation using v_m=5 mm/s, D_{M-M} [i]=7.5 mm and H_s=2 mm. Movie S2. Verification of Movie S1.

Author Contributions Lidong Zhao: investigation, methodology, simulation and experiment, writing—original draft, modification. Yan Zhang: build a numerical model and writing review. Lifang Wu: writing review and editing, supervision, project administration, funding acquisition. Zhi Zhao: writing review and editing, supervision. Zening Men: software. Feng Yang: participated in experiments. All authors read and approved the final manuscript.

Funding This work is partially supported by the Key projects of science and technology plan of the Beijing Municipal Commission of Education (KZ202110005007) and the Special plan of the National key R&D Program of international cooperation in science and technology innovation between governments (2018YFE0197100).

Data Availability The datasets used or analyzed during the current study are available from the corresponding author on reasonable request.

Code availability The custom code in the current study of slice analyse can be obtained from the corresponding author upon reasonable request.

Declarations

Ethics approval This paper is new and has not been published, accepted, or submitted to any other journal.

Consent to participate Not applicable

Consent to publication Not applicable

Competing interests The authors declare no competing interests.

References

1. Leung YS, Kwok TH, Li X, Yang Y, Wang CCL, Chen Y (2019) Challenges and status on design and computation for emerging additive manufacturing technologies. J Comput Inf Sci Eng 19(2):021,013.1–021,013.21. https://doi.org/10.1115/1.4041913
2. Ngo TD, Kashani A, Imbalzano G, Nguyen KTQ, Hui D (2018) Additive manufacturing (3D printing): a review of materials, methods, applications and challenges. Compos Part B 143:172–196. https://doi.org/10.1016/j.compositesb.2018.02.012
3. Tan LJ, Zhu W, Zhou K (2020) Recent progress on polymer materials for additive manufacturing. Adv Funct Mater 30(43):2003,062–2003,115. https://doi.org/10.1002/adfm.202003062
4. Calignano F, Manfredi D, Ambrosio EP, Biamino S, Lombardi M, Atzeni E, Salmi A, Minetola P, Iuliano L, Fino P (2017) Overview on additive manufacturing technologies. Proc IEEE 105(4):1–20. https://doi.org/10.1109/JPROC.2016.2625098
5. Kianian B (2016) Wohlers report 2016: 3D printing and additive manufacturing state of the industry, Annual Worldwide Progress Report : Chapter title: The Middle East
6. Zhao Z, Tian X, Song X (2020) Engineering materials with light: recent progresses in digital light processing based 3D printing. J Mater Chem C 8:13,896–13,917. https://doi.org/10.1039/D0TC03548C
7. Wu J, Guo J, Linghu C, Lu Y, Song J, Xie T, Zhao Q (2021) Rapid digital light 3D printing enabled by a soft and deformable hydrogel separation interface. Nat Commun 12(1):6070–6078. https://doi.org/10.1038/s41467-021-26386-6
8. Beer M, Laan H, Cole MA, Whelan RJ, Scott TF (2019) Rapid, continuous additive manufacturing by volumetric polymerization inhibition patterning. Sci Adv 5(1):8723. https://doi.org/10.1126/sciadv.aau8723
9. Chen L, Zheng Y, Meng X, Wei G, Li Z (2020) Delayed thiol-epoxy photopolymerization: a general and effective strategy to prepare thick composites. ACS Omega 5(25):15,192–15,201. https://doi.org/10.1021/acsomega.0c01170
10. Tumbleston JR, Shirvanyants D, Ermoshkin N, Janusziewicz R, Johnson AR, Kelly D, Chen K, Pinschmidt R, Rolland JP, Ermoshkin A (2015) Additive manufacturing. Continuous liquid interface production of 3D objects. Science 347(6228):1349–1352. https://doi.org/10.1126/science.aaa2397
11. Walker DA, Hedrick JL, Mirkin CA (2019) Rapid, large-volume, thermally controlled 3D printing using a mobile liquid interface. Science 366(6463):360–364. https://doi.org/10.1126/science.aax1562
12. Wu L, Dong Z, Du H, Li C, Fang NX, Song Y (2018) Bioinspired ultra-low adhesive energy interface for continuous 3D printing: reducing curing induced adhesion. Research 2018(1):4795,604–4795,613. https://doi.org/10.1155/2018/4795604
13. Li X, Mao H, Pan Y, Yong C (2019) Mask video projection-based stereolithography with continuous resin flow. J Manuf Sci Eng 141:081,007. https://doi.org/10.1115/1.4043765
14. He H, Pan Y, Feinerman A, Xu J (2018) Air-diffusion-channel constrained surface based stereolithography for three-dimensional printing of objects with wide solid cross sections. J Manuf Sci Eng-Trans Asme 140(6):061,011–1–061,011–9. https://doi.org/10.1115/1.4039440
15. Quan H, Zhang T, Xu H, Luo S, Nie J, Zhu X (2020) Photo-curing 3D printing technique and its challenges. Bioact Mater 5(1):110–115. https://doi.org/10.1016/j.bioactmat.2019.12.003
16. Liu Z, Li Y, Wu L, Cui K, Yan J, Yu H (2021) Model guided DLP 3D printing for solid and hollow structure. In: 14th International conference on human system interaction, HSI 2021, July 8, 2021 - July 10, 2021. https://doi.org/10.1109/HSI52170.2021.9538633
17. Li Y, Wu L, Cui K, Yang F, Zhao L (2022) Model-guided 3D printing combining continuous and layer-wise manufacturing. J Integr Technol 11(1):88–96. https://doi.org/10.12146/j.issn.2095-3135.20210930001
18. Wang Q, Sun Y, Guo B, Li P, Li Y (2019) CFD analysis and prediction of suction force during the pulling-up stage of the continuous liquid interface production process. AIP Adv 9(1):015,225–1–015,225–7. https://doi.org/10.1063/1.5080516
19. Lee MH, Chen SI, Chen WH, Mao Y (2019) A layer-based mesh generator and scheme for 3D printing simulation. CMES 120(2):363–374. https://doi.org/10.32604/cmes.2019.06476
20. Li Y, Mao Q, Yin J, Wang Y, Fu J, Huang Y (2021) Theoretical prediction and experimental validation of the digital light processing (DLP) working curve for photocurable materials. Addit Manuf 37:101,716–101,725. https://doi.org/10.1016/j.addma.2020.101716
21. Brighenti R, Cosma MP, Marsavina L, Spagnoli A, Terzano M (2021) Multiphysics modelling of the mechanical properties in polymers obtained via photo-induced polymerization. Int J Adv Manuf Technol 117(1-2):481–499. https://doi.org/10.1007/s00170-021-07273-2

22. Wang Q, Wang J, Zhang Y, Liu Y, Zheng J, Li Y (2021) Multi-physics simulation and experimental study of the reaction kinetics process of oxygen inhibition zone formation in constrained-surface stereolithography process. Addit Manuf 47:102,280–102,291. https://doi.org/10.1016/j.addma.2021.102280
23. Zhao P, He Y, Trindade GF, Baumers M, Conceptualisation RW (2021) Modelling the influence of UV curing strategies for optimisation of inkjet based 3D printing. Mater Des 208:109,889. https://doi.org/10.1016/j.matdes.2021.109889
24. Li J, An X, Liang J, Zhou Y, Sun X (2022) Recent advances in the stereolithographic three-dimensional printing of ceramic cores: Challenges and prospects. J Mater Sci Technol 117:79–98. https://doi.org/10.1016/j.jmst.2021.10.041
25. Kim SH, Yamashiro M, Yoshida A (2010) A simple two-way coupling method of BEM and VOF model for random wave calculations. Coast Eng 57(11-12):1018–1028. https://doi.org/10.1016/j.coastaleng.2010.06.006
26. Zhang Y, Lyu L, Li P (2022) An optimized volume of fluid method for modelling three-dimensional debris flows. Implementation in OpenFoam, validation, and application in the Aiwa Watershed, Beijing. Comput Geotech 144:104,651–104,664. https://doi.org/10.1016/j.compgeo.2022.104651
27. Wu C, Ma G (2005) On the boundary slip of fluid flow. Science in China, Series G 48(2):178–187. https://doi.org/10.1360/03yw0304
28. Krishnamoorthy S, Wadnap S, Noorani B, Xu H, Xu C (2020) Investigation of gelatin methacrylate working curves in dynamic optical projection stereolithography of vascular-like constructs. Eur Polym J 124:109,487. https://doi.org/10.1016/j.eurpolymj.2020.109487
29. Deng T, Liu W, Xie W, Huang J, Tang A (2021) Mask image grayscale regulation for projection stereolithography in tissue engineering. Int J Adv Manuf Technol 113(9-10):3011–3026. https://doi.org/10.1007/s00170-021-06756-6
30. Wu L, Zhao L, Jian M, Mao Y, Yu M, Guo X (2018) EHMP-DLP: multi-projector DLP with energy homogenization for large-size 3D printing. Rapid Prototyp J 24(9):1500–1510. https://doi.org/10.1108/RPJ-04-2017-0060